Prediction of cooling rate and microstructure in laser spot welds

A. De, C. A. Walsh, S. K. Maiti and H. K. D. H. Bhadeshia

Theoretical and experimental investigations have been carried out to examine the influence of laser power and on time on the weld thermal cycle and weld metal microstructure and hardness during laser spot welding of low alloy steel. A transient heat transfer model that takes into account the temperature dependence of material properties and latent heat of phase transformation is employed to simulate thermal cycles and cooling rates experienced by the material under various combinations of power and on times. Two models for predicting the microstructure and hardness of the weld pool metal from the cooling rates are used to evaluate the results. *STWJ/370*

Professor De (amit@me.iitb.ac.in) and Professor Maiti are in the Mechanical Engineering Department, Indian Institute of Technology, Bombay, Powai, Bombay 400 076, India. Dr Walsh and Professor Bhadeshia are in the Department of Materials Science and Metallurgy, University of Cambridge, Pembroke Street, Cambridge CB2 3QZ, UK. *Manuscript received 1 October 2002; accepted 7 January 2003.*

INTRODUCTION

Laser beam welding is finding an increasing number of applications in industry and in research[1–8] because it can lead to an increase in productivity, reduction in distortion and is amenable to automation. The cooling rate associated with laser welding is a key feature in determining the properties of any resulting welds, and is a function of the laser power, the interaction time between the beam and the substrate, the weld pool dimensions and the absorptivity and thermophysical properties of the substrate. Measurement of the cooling rates can be difficult for laser welds and hence there has been a trend to develop models.

Analytical representations of heat flow in laser beam welding, reported by Swift-Hook and Gick[9] followed by Andrews and Atthey[10] and Metzbower,[11] were formulated by approximating the beam as a point or line heat source. Kaplan[12] calculated the keyhole profile using a point by point determination of the energy balance along the keyhole wall, locally solving the energy balance equation and representing the laser as a line heat source. Guo and Kar[13] used a Gaussian surface heat source but temperature independent material properties; they also neglected any latent heat of transformation and made a number of other geometric approximations. These difficulties were overcome by numerical methods[14–17] but the assumption of a Gaussian intensity distribution applied only to the top surface is not appropriate for high power lasers, which lead to the formation of a keyhole with the transport of heat well below the surface. Occasionally, this was tackled by assuming that the beam intensity reaching a certain depth follows the Beer–Lambert law, $q_z = q_0 e^{-\beta z}$, where β is the absorption coefficient and q_z and q_0 are the intensities at depth z and on the top surface, respectively. In general, β was set by trail and error. Furthermore, a 'Gaussian rod' type, volumetric heat source was proposed,[18] however, its suitability was not tested for various possible weld pool shapes depending on the process parameters, such as laser power, weld speed, pulse on time, and absorptivity variation.

Goldak *et al.*[19,20] reported a finite element based heat flow analysis with a distributed 'double-ellipsoidal' type, volumetric energy source, applicable to high energy density welding and capable of accommodating a variety of pool shapes. The method does, however, require a prior knowledge of the weld pool shape in order to define the heat source. In another finite element method based model,[21] the heat flux was assumed to have a conical distribution, which was arrived upon by means of very specialised experiments.

Since it is well established that the cooling rate influences the microstructure and properties of the weld metal,[22–27] it was the purpose of the present work to combine a finite element based heat flow model for laser spot welds, with a microstructure model for steel welds, to allow the hardness of spot welds to be estimated as a function of the welding parameters and the chemical composition of the steel. The microstructure models considered here have been documented extensively elsewhere[22–26,28–32] and hence will only be discussed in context. Similarly, many models have been published which couple thermal models with microstructure calculations;[33–37] the distinction here is that the present authors apply the heat flow and microstructure theory to laser spot welds in lean automobile steels.

THEORETICAL FORMULATION

The equation for transient heat conduction in two-dimensional cylindrical coordinates is given by

$$\frac{1}{r}\frac{\partial}{\partial r}\left(rK\frac{\partial T}{\partial r}\right)+\frac{1}{r}\frac{\partial}{\partial z}\left(rK\frac{\partial T}{\partial z}\right)+\dot{Q}=sc\frac{\partial T}{\partial t} \quad (1)$$

where r and z are radial and axial coordinates, s, c and K are the density, specific heat and thermal conductivity of the material respectively, T and t refer to temperature and time and $\dot{Q}$ refers to the rate of internal heat generation per unit volume. The essential and natural boundary conditions are expressed respectively as

$$T = T_{S_1} \quad \text{(on the portion of the boundary } S_1) \quad (2)$$

$$K_n\frac{\partial T}{\partial n} - q + h(T-T_0) + \sigma\varepsilon(T^4 - T_0^4) = 0$$

$$\text{(on the portion of the boundary } S_2 \text{ and } t>0) \quad (3)$$

Incidentally, S_2 represents those surfaces that may be subjected to radiation, convection and imposed heat fluxes q, K_n represents thermal conductivity normal to the surface, T_0 the ambient temperature, h the convective heat transfer coefficient, ε the emissivity and σ the Stefan–Boltzmann

constant for radiation. Instead of considering the radiation term in the boundary condition, the effect of radiation and convection is considered together through a 'lumped' heat transfer coefficient[21] as

$$h = 2{\cdot}4 \times 10^{-3} \varepsilon T^{1{\cdot}61} \quad \ldots \quad (4)$$

Due to the axial symmetry, the radial heat transfer across the laser beam axis (the symmetry line) is taken as zero, i.e. $\partial T/\partial r = 0$.

The finite element discretisation has been carried out using a three node, ring type solid element[37,38] with triangular cross-section. Within an element, temperature can be expressed as

$$\{T\} = [N_i N_j N_k]\{\mathrm{T^e}\} \quad \ldots \quad (5)$$

where N_i, N_j and N_k are the shape functions (based on nodal coordinates of the element) respectively for the ith, jth and kth nodes of the element and $\{T^\mathrm{e}\}$ is the elemental temperature vector having three nodal temperatures as its components. Equation (1) is first discretised using Euler's variational approach and the discretised equation can be stated as

$$[H]\{T\} + [S]\frac{\partial}{\partial t} + \{F\} = 0 \quad \ldots \quad (6)$$

where $[H]$ is the thermal conductivity matrix, $[S]$ is the thermal capacity matrix and $\{F\}$ is the load vector. Galerkin's method in weighted residue technique has been applied further to solve equation (6) in the time domain as

$$\left(\frac{2}{3}[H] + \frac{1}{\Delta t}[S]\right)(\{T\})_{\mathrm{n}+1} + \left(\frac{1}{3}[H] - \frac{1}{\Delta t}[S]\right)(\{T\})_{\mathrm{n}} + \frac{2}{\Delta t^2}\int_0^{\Delta t}\{F\}t\,\mathrm{d}T = 0 \quad \ldots \quad (7)$$

where t is the time variable, Δt is the time increment, $\{T\}_\mathrm{n}$ and $\{T\}_{\mathrm{n}+1}$ are the nodal temperature vectors corresponding to the beginning (i.e. nth) and the end (i.e. $(n+1)$th) of the time increment Δt, respectively. The elements of $[H]$, $[S]$ and $\{f\}$ matrices are given as

$$h_{\mathrm{ij}}^{\mathrm{e}} = \iint \left(K \cdot \frac{\partial N_\mathrm{i}}{\partial r} \cdot \frac{\partial N_\mathrm{j}}{\partial r} + K \cdot \frac{\partial N_\mathrm{i}}{\partial z} \cdot \frac{\partial N_\mathrm{j}}{\partial z}\right) 2\pi r\, dr\, dz \quad (8)$$

$$s_{\mathrm{ij}}^{\mathrm{e}} = \iint_{\mathrm{v}} N_\mathrm{i} sc N_\mathrm{j}\, 2\pi r\, dr\, dz \quad \ldots \quad (9)$$

$$\{f_\mathrm{i}^{\mathrm{e}}\} = -\iint_{\mathrm{v}} \left(\dot{Q} - sc\frac{\partial T}{\partial t}\right) N_\mathrm{i}\, 2\pi r\, dr\, dz \quad \ldots \quad (10)$$

The standard derivation of equation (1) in the form of equation (7) is available in standard finite element books and hence is not repeated here. The latent heat of melting and solidification is included in this simulation through an increase or decrease in the specific heat of the material. The specific heat c is expressed as follows

$$\left.\begin{array}{ll} c = C_1 & \text{for } T \leqslant T_\mathrm{S} \\ c = C_2 & \text{for } T \geqslant T_\mathrm{L} \\ c = C_\mathrm{m} = \frac{\lambda}{T_\mathrm{L} - T_\mathrm{S}} + \frac{C_1 + C_2}{2} & \text{for } T_\mathrm{S} \leqslant T \leqslant T_\mathrm{L} \end{array}\right\} \quad (11)$$

where λ is latent heat (272·156 kJ kg^{-1} for steel), T_S and T_L are solidus and liquidus temperatures, respectively. For an element of volume undergoing a phase change the specific heat is obtained as a weighted average of the associated specific heats, namely C_1 and C_m (for solid to mushy state or vice versa), C_m and C_2 (for mushy to liquid state or vice versa) or C_1, C_m and C_2 (for a jump from solid to liquid state or vice versa).[37]

Calculation of weld dimensions and cooling rate

The present theoretical study is based on measured fusion zone dimensions and known material data for diode laser spot welds in a single sheet of metal. The experimental details are reported elsewhere.[39] The heat source was a 2·2 kW Jold 1000 diode laser with a beam spot of diameter of 1·0 mm. The beam was focussed normally onto the top surface of a 2·0 mm thick D52X low carbon steel sheet using a lens of 50 mm focal length. The material composition is given in Table 1. Three levels of beam powers, namely 1·0, 1·4 and 2·23 kW, and on times varying in the range 0·15–2·65 s were investigated (Table 2). Argon was used as the shielding gas in all cases.

For the purpose of modelling these laser welds, a rectangular region of 15 mm (width) by 2 mm (thickness) is finely discretised (meshed) into divisions of 0·1 mm along the thickness direction.[38] Along the width direction, a division of 0·1 mm is used up to a distance of 5 mm and onwards a division of 0·2 mm is used for the rest of the length. A three node, triangular ring type element is used.[37,38] The time span of the transient analysis includes the on time of a single laser pulse and the subsequent cooling stage. The analysis is carried out through a number of small time steps of 0·001 s duration. Within each time step, a number of iterations is performed to achieve a convergence criterion of 1% (the difference in nodal temperature between two successive iterations).[38] Figure 1 shows the temperature dependent material properties used in the calculations. Figure 2 shows schematically the zone used for analysis and the boundary conditions applied. The solidus and liquidus temperatures are taken as 1480 and 1500°C, respectively. The liquidus temperature is actually used to estimate the fusion boundary and a reasonable

Table 1 Chemical compositions of workpiece material, wt-% (Ref. 39)

C	Si	Mn	Cr	Mo	Ni	V	N	Fe
0·07	0·10	0·92	0·04	<0·01	0·03	<0·01	0·005	Bal.

Table 2 Incident laser powers and on times used in experiments and corresponding cooling rate parameters, C_1 and C_2, determined from numerical analyses

	Laser Power, W							
	1000		1400			2230		
On time, s	C_1	C_2	On time, s	C_1	C_2	On time, s	C_1	C_2
0·15	94·816	166·17	0·15	105·98	179·16	0·15	18·007	145·15
0·65	19·848	159·99	0·65	20·218	184·52	0·165	16·016	144·27
1·15	23·789	232·77	1·15	27·923	277·99	0·180	14·224	147·22
1·65	30·887	306·58	1·65	41·344	388·11	0·195	10·802	141·78
2·15	43·286	407·81	2·15	56·702	520·94	0·210	9·4920	144·98
2·65	57·435	529·91	2·65	61·998	583·07	0·225	8·0715	145·03

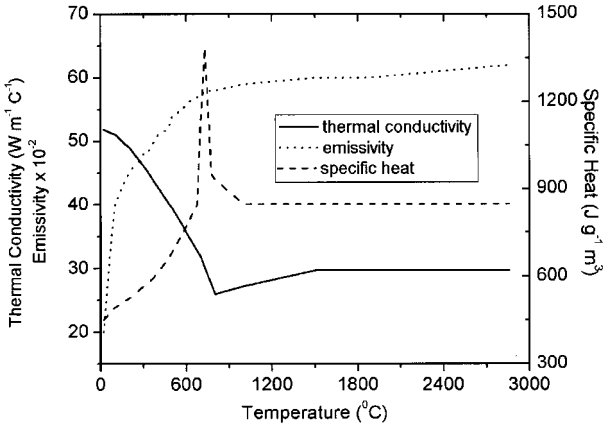

1 Temperature dependent thermal conductivity and specific heat of material

agreement[38] was found between the measured and the calculated weld dimensions using the 1500°C isotherm as the fusion zone boundary (*see* Figs. 4 and 5). The calculated equilibrium liquidus temperature[40] for the steel used is in fact 1520°C, but the weld does not cool under equilibrium conditions, hence the use of 1500°C may be a good approximation. The latent heat λ is taken as 272·156 kJ kg^{-1}. During the analysis, whenever the temperature of a node exceeds the boiling point of the steel (2800°C), it is allowed to remain in the mesh at the boiling temperature and is not considered further in the analysis until cooling starts after removal of the laser beam.

The volumetric heat input due to the laser beam is adapted from the 'double-ellipsoidal'[19,20] form (Fig. 3)

$$q(x,y,z,t)=\frac{6\sqrt{3}f_{1,2}Q}{abc_{1,2}\pi\sqrt{\pi}}\ e^{-3\frac{x^2}{a^2}}e^{-3\frac{y^2}{b^2}}e^{-3\frac{(z-v(\tau-t))^2}{a^2}} \qquad (12)$$

where Q is the intensity due to the heat source and given by laser power multiplied by absoptivity, v is the welding velocity, $2a$ is the weld bead width, b is the penetration, and c_1 and c_2 are the extent of the heat source from its centre in the front and rear, respectively (Fig. 3). The representation, in effect, becomes a combination of two half ellipsoids (one at the front of the centre of the heat source and the other at the rear), the intensity of the heat source being distributed in a Gaussian manner within each half ellipsoid. The front ellipsoid is defined by a set of axes c_1, $2a$ and b, while the rear one is defined by c_2, $2a$ and b. The constants f_1 and f_2 are associated with the front and rear region, respectively, in an approximate manner as $f_1+f_2=2$. The complete

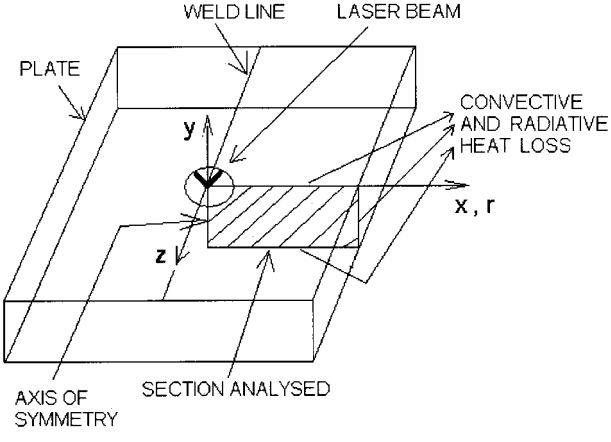

2 Transverse section considered in present analysis

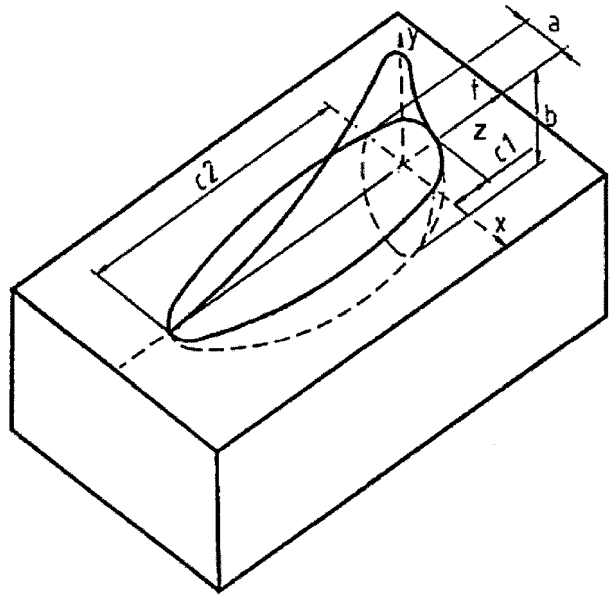

3 Schematic presentation of 'double-ellipsoidal' distribution of laser beam

representation not only accounts for a volumetric heat input well inside the material but also considers the fact that in the case of a relative motion between the heat source and the material, there will be an asymmetry in the magnitude of heat input between the front region and the rear region at the centre of the heat source. Since the present work involves laser spot welding, a two-dimensional stationary form of equation (12) is utilised with $v=0$, $z=0$ and $a=c_1=c_2$ which is the focal radius of the laser beam. The value of b is taken to be the sheet thickness for 1·4 and 2·23 kW and 0·60 mm for 1·0 kW laser power. The absorptivity is fixed at 50% below the boiling point of the steel in the case of 1·4 and 2·23 kW laser power and 30% in the case of 1·0 kW power. The need for different absorptivity data may stem from the fact that absorptivity greatly depends on temperature and temperature is dictated by the laser power and other process parameters. This rather imposes a problem in choosing a single absorptivity value for different laser powers during theoretical simulation. This problem is further compounded by the fact that equation (12) needs prior selection of the parameters a and b. In the present work, all these values are arrived at by comparing the calculated weld dimensions against the experimental data[39] as described elsewhere.[38]

Figures 4 and 5 show the comparison of calculated and measured weld bead dimensions for different combinations of laser power and on times. In both Figs. 4 and 5, the lower x axis corresponds to the on times for 1·0 and 1·4 kW laser power and the upper x axis corresponds to the on times for 2·23 kW laser power. A detailed discussion on these results has already been presented.[38] The calculated thermal history (i.e. time–temperature relationship) of the molten weld pool is utilised to calculate the cooling rate (dT/dt; where T is temperature and t is time) of the weld pool as a function of its temperature. Figure 6*a*–*c* shows the cooling rate as a function of mean weld pool temperature for different combinations of laser power and on times. It is clear that the cooling rate at any instantaneous weld pool temperature is influenced by both laser power and on time. For example, the cooling rate at 1400°C and short laser on times (0·15 s) is $\sim 10^5$ K s^{-1} for all three laser powers. The calculations indicate a slight reduction in cooling rate with increasing laser power from $4{\cdot}5\times10^5$ K s^{-1} at 1·0 kW to $2{\cdot}6\times10^5$ K s^{-1} at 1·4 kW (Fig. 6*a* and *b*), which, although

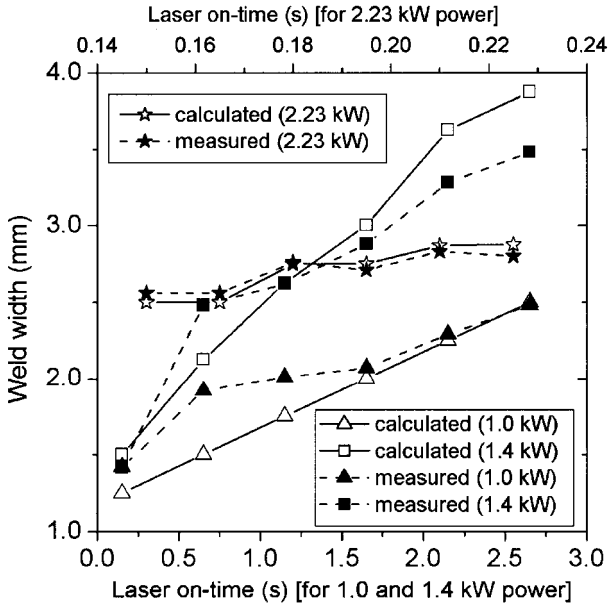

4 Comparison of calculated and measured weld pool width as measured on upper surface

small, follows the expected trend that the cooling rate at a particular location is a function of the laser power. With 2·23 kW laser power, however, the calculated cooling rate at 1400°C did not reduce further and is $2{\cdot}8\times10^5$ K s^{-1} (Fig. 6*c*). As the laser on time increases from 0·15 to 2·65 s with 1·0 kW and 1·4 kW laser power, the cooling rates at 1400°C decrease to $9{\cdot}0\times10^5$ and $7{\cdot}0\times10^5$ K s^{-1}, respectively (Fig. 6*a* and *b*). With 2·23 kW laser power, on times higher than 0·225 s were not considered experimentally or in the numerical calculation since full penetration had already been achieved. In this case, the cooling rate at 1400°C reduces only slightly as the on time increases from 0·15 s ($2{\cdot}8\times10^5$ K s^{-1}) to 0·225 s ($1{\cdot}25\times10^5$ K s^{-1}) (Fig. 6*b*). Similar observations can also be made at relatively lower temperatures. This shows that the cooling rate at a certain temperature reduces readily with an increase in on time, while an increase in laser power can

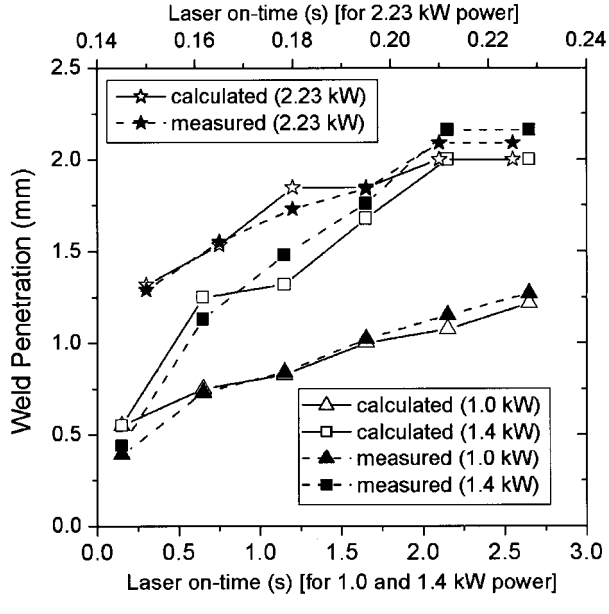

5 Comparison of calculated and measured weld penetration

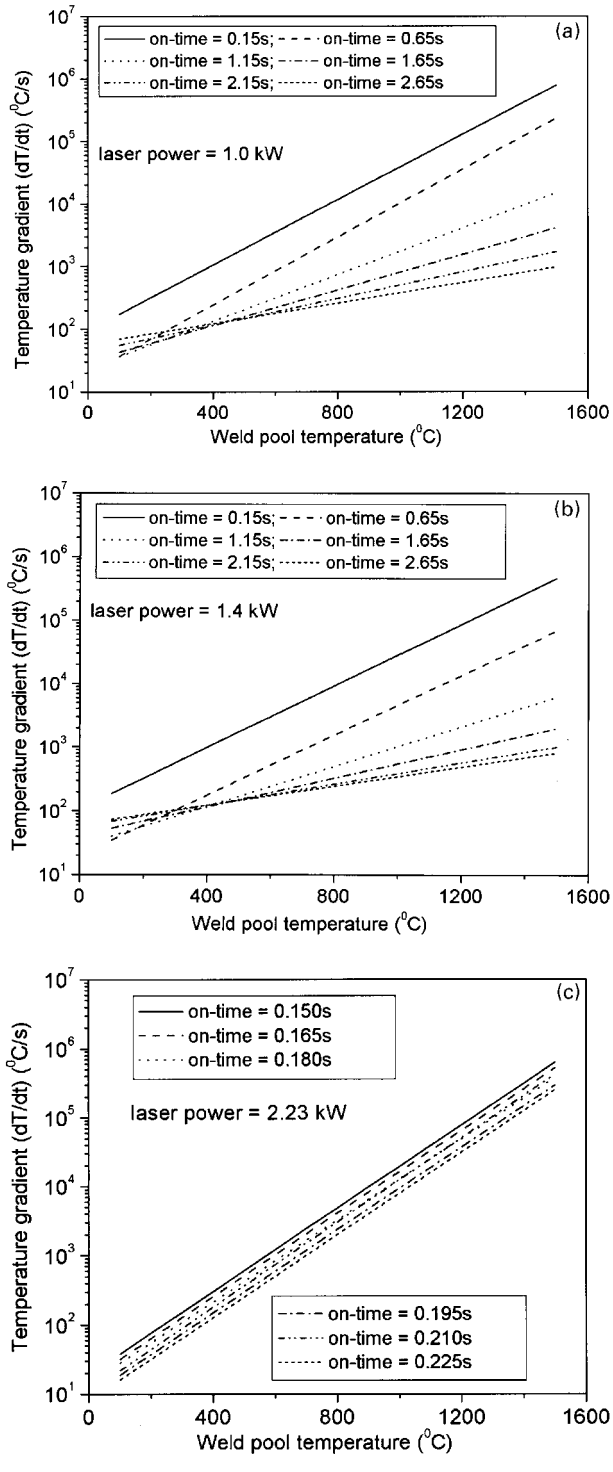

a 1·0 kW; *b* 1·4 kW; *c* 2·23 kW

6 Variation of cooling rate with weld pool temperature for given laser powers

slow down the cooling rate only to a certain extent. It is also true that the cooling rate drops sharply with a decrease in temperature in all the cases (Fig. 6).

The cooling rate calculated using the finite element based heat transfer model is next fitted to an equation of the form

$$\frac{\mathrm{d}T}{\mathrm{d}t} = -C_1 e^{\frac{T}{C_2}} \quad \ldots\ldots\ldots\ldots\ldots\ldots \quad (13)$$

where $\mathrm{d}T/\mathrm{d}t$ refers to the cooling rate (K s^{-1}), T is the temperature variable (°C), C_1 and C_2 are constants which are given in Table 2 for each combination of laser power

and on times considered. Although the trends represented by the cooling rate curves in Fig. 6 inherently suggest an exponential behaviour of cooling rate with instantaneous temperature (equation (13)), this can also be manifested from the basic analytical solution of the heat conduction equation. In two-dimensions, the temperature field T due to an instantaneous stationary line source of strength Q at time $t=0$ is analytically represented as[41]

$$T-T_0=\frac{Q}{4\pi\kappa g}\exp\left(\frac{-(x^2+y^2)}{4\kappa t}\right) \quad \ldots\ldots (14)$$

where T_0 is the ambient temperature, κ is the temperature independent thermal diffusivity ($K/\rho s$, where K refers to thermal conductivity, s specific heat and ρ density) and Q is the amount of heat liberated per unit line length. Assuming the line heat source produces heat for a time τ, it is possible to estimate the temperature field in a spot weld by $Q\rho s=(\eta q\Delta t)/g$ where η is the energy transfer efficiency (absorptivity), q is the power of the incident laser and g is the penetration depth of the laser beam (uniform absorption of the beam is assumed over this depth). Integrating equation (14) over time t' from 0 to τ gives

$$T-T_0=\int_0^{\tau}\frac{\eta q\,\mathrm{d}t'}{4\pi Kg(t-t')}\exp\left(-(x^2+y^2)/4\pi\kappa(t-t')\right) \quad (15)$$

It can easily be shown that at the centre of the weld ($x=0$, $y=0$) and for times $t>\tau$, the solutions for temperature and cooling rate, in terms of time and temperature, respectively, are

$$T-T_0=\frac{\eta q}{4\pi Kg}\ln\left(\frac{t}{t-\tau}\right) \quad \ldots\ldots (16)$$

$$\frac{\mathrm{d}T}{\mathrm{d}t}=-\frac{\eta q}{4\pi Kg\tau}\frac{(\exp(4\pi Kg(T-T_0)/\eta q)-1)^2}{\exp(4\pi Kg(T-T_0)/\eta q)} \quad (17)$$

So when $T-T_0\gg\eta q/4\pi Kg$, equation (17) simplifies to the form

$$\frac{\mathrm{d}T}{\mathrm{d}t}=-C_1e^{\mathrm{T}/C_2} \quad \ldots\ldots (18)$$

where

$$C_1=\frac{\eta q}{4\pi Kg\tau}\exp(-4\pi KgT_0/\eta q)$$

and

$$C_2=\frac{\eta q}{4\pi Kg}$$

At lower temperatures, $T-T_0\ll\eta q/4\pi Kg$, equation (17) reduces to

$$\frac{dT}{dt}=\frac{4\pi Kg}{\eta q\tau}(T-T_0)^2 \quad \ldots\ldots (19)$$

Although $\eta q/4\pi Kg$ is typically $\sim$1000°C or more, the results of the finite element analysis have been found to conform to the form of equation (18), with values for both C_1 and C_2 which are considerably lower than the analytical values. A useful comparison of the cooling curves can be made by calculating $t_{8/5}$, the time taken for the weld pools to cool from 800 to 500°C. This is significant since it corresponds to the temperature regime over which austenite to ferrite phase transformations take place. The ratio of $t_{8/5}$ from the finite element calculations to the corresponding value from equation (16) is shown for each weld in Fig. 7, plotted as a function of the absorbed energy. In the analytical calculations g is taken as the experimentally measured penetration (Figs. 4 and 5).

In some cases, notably low power and low absorbed energy, the cooling times given by the finite element calculations are lower than predicted by the analytical expressions. A likely reason for this discrepancy is that in these cases, the welds have only partially penetrated the metal sheets. This actually sets up non-uniform heat transfer in the radial direction at a different depth in the sheet, which cannot be accounted for using an uniform line heat source in the thickness direction as used in the analytical calculation. The finite element calculation, however, uses a heat source that decays slowly in the thickness direction to a finite magnitude and thus permits a strong and transient heat transfer both in the radial and the axial direction, resulting in faster cooling rates and lower cooling times.

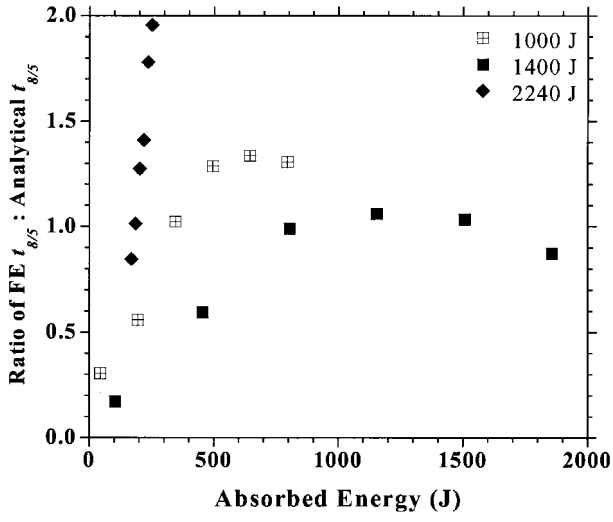

7 Ratio of $t_{8/5}$ obtained using finite element analysis to $t_{8/5}$ obtained from simple analytical model where $t_{8/5}$ is time taken by weld pool to cool from 800 to 500°C

At the highest incident laser power (2·24 kJ), a keyhole is able to form, resulting in narrower weld pools, which completely or almost completely penetrate the metal sheet. The analytical formula ought to be most applicable to such welds, however, the finite element calculations give cooling times of up to two times higher than the values obtained from the analytical equation. Possible reasons for a slower release of heat from the weld pool include the finite size of the incident laser beam, which limits the maximum temperature reached at the centre of the weld pool, the release of latent heat during solidification of the molten metal and a consideration of the temperature dependence of the material properties, all of which are modelled by the finite element calculations and ignored by the analytical model. It should be noted that in the finite element calculation, the maximum temperature reached at the centre of weld pool is also restricted up to the material boiling temperature since it is felt not appropriate to apply the simple heat conduction equation to the vapour state of material.[21]

At lower incident laser powers and higher absorbed energies, the welding process is dominated by conductive heating, producing weld pools, which are broad but only partially or just fully penetrating. The accuracy of the analytical calculations suffer from both of the above competing effects which, it appears, largely compensate one another, giving reasonable agreement in the calculated values of $t_{8/5}$ from the two models.

Estimation of weld microstructure and hardness

The finite element model described above is essential for obtaining a realistic description of the weld thermal cycle (i.e. rate of heating and subsequent cooling of weld pool) and pool size. The estimation of weld microstructure requires an input of cooling rate. Before discussing the theoretical models for the estimation of weld microstructure, a brief explanation is given of the phases to be

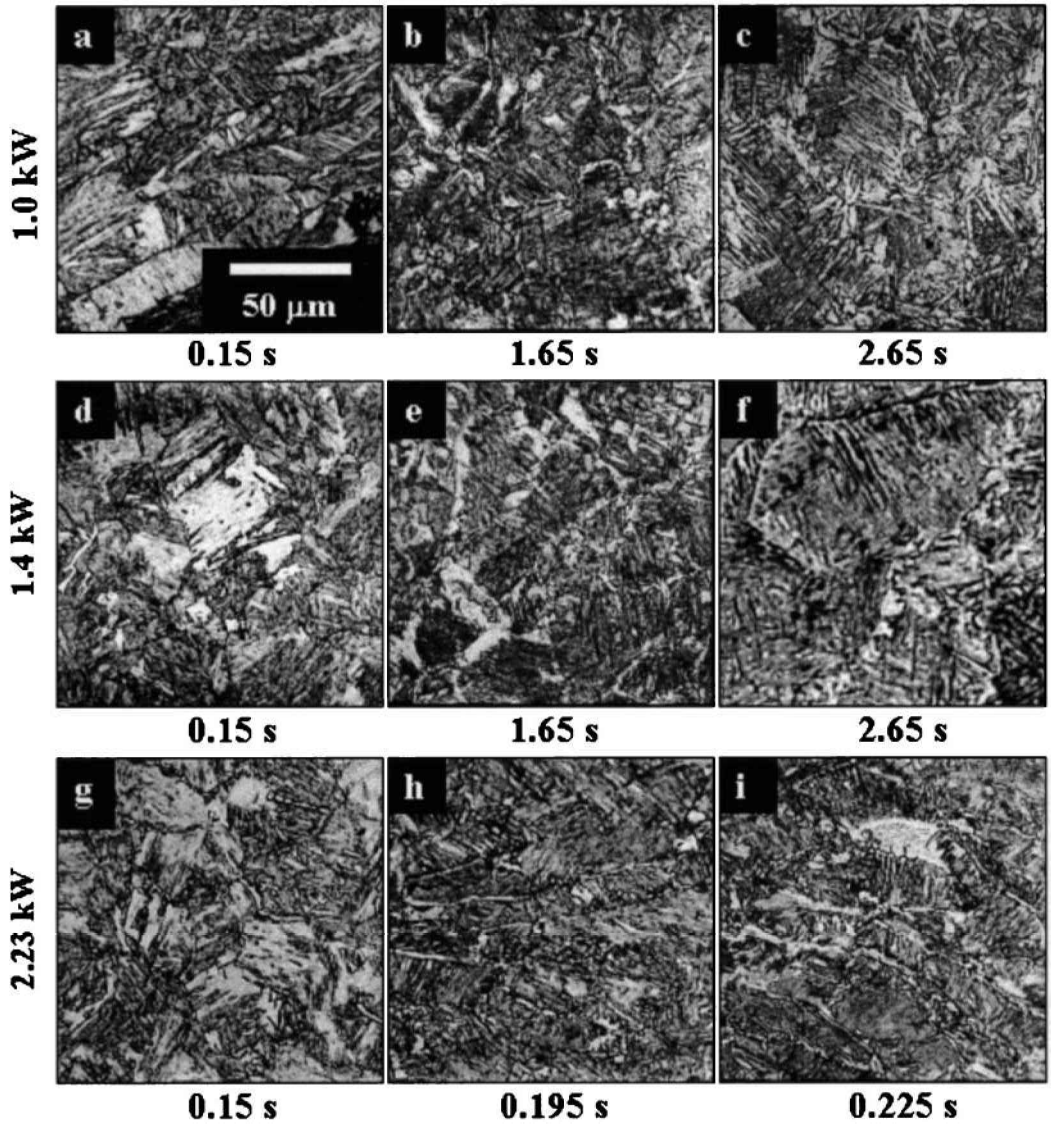

8 Observed microstructure in weld pool of spot welds for given laser powers and laser on times

expected in the class of steel considered here.[22] The weld should solidify first to columnar grains of δ ferrite, which then undergo solid state transformation into corresponding columnar grains of austenite. Further cooling below the equilibrium Ae_3 temperature causes the austenite to begin transformation into a variety of ferritic phases.

Allotriomorphic ferrite is the first phase to form, by the reconstructive transformation of austenite, on cooling below Ae_3. The ferrite has a relatively low solubility for carbon and hence the carbon is partitioned into the residual austenite during the course of the transformation. Its growth is therefore frequently controlled by the diffusion of carbon into the austenite at the transformation front. Allotriomorphic ferrite grows in the form of layers, which tend to decorate the austenite grain surfaces; during transformation carbon accumulates ahead of the ferrite causing growth to slow as the layer thickens. Conversely, Widmanstätten ferrite grows in the form of plates or laths, permitting carbon to be partitioned to the sides. This allows the plates to lengthen at a steady rate, which is much more rapid than the thickening of allotriomorphs. Bainite and acicular ferrite are also platelike but have a different mechanism of transformation and hence occur at lower temperatures, sometimes accompanied by the precipitation of cementite. Any remaining austenite then either decomposes into martensite or is retained in small quantities in the microstructure. In general the lower the transformation temperature, the higher the hardness and strength of the austenite transformation product. The overall hardness of the weld metal depends on the relative proportions of each of these different structural forms.

The microstructures of the spot welds were examined after polishing and etching in a 2% nital solution. The hardness of each weld was taken as the mean of three measurements made using a Mitutoyo MVK-H2 machine for hardness testing. Figure 8 shows the observed microstructures as a function of increasing laser on time and incident laser power. In each case the weld produced using the shortest laser on time consists almost entirely of martensite, although the growth of some allotriomorphic ferrite at the prior austenite grain boundaries is evident at the highest laser power. As the laser on time is increased, the cooling rate decreases and more allotriomorphic and Widmanstätten ferrite forms. This is accompanied by a decrease in hardness with increasing laser on time as shown in Fig. 9; the 'error bars' in Fig. 9 indicate observed scatter.

Two different computer programs have been used to model and predict the microstructure in the fusion zone of the laser spot welds. The first program (Model 1) is based on a model due to Bhadeshia, Svensson and Gretoft,[22–26,42] involving phase transformation theory including calculated phase diagrams, transformation temperatures, growth rates

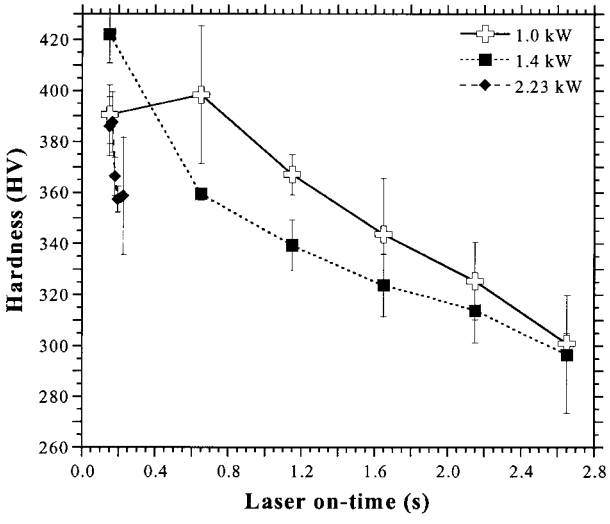

9 Measured hardness of weld pool metal as function of laser on time

of individual phases and time–temperature–transformation curves for the estimation of the fractions of allotriomorphic and Widmanstätten ferrite, but also includes models for the calculation of the fractions of bainite and acicular ferrite,[28] and of martensite and retained austenite[29] in the final weld microstructure. Corresponding calculations of yield strength and hardness of the fusion zone metal are also implemented.[22,30,31] This model has been mostly used in the past for arc welding processes. The program requires as inputs the austenite grain size, the chemical composition of the steel and the cooling curve of the fusion zone over the temperature range in which the solid state transformation of austenite occurs (800–500°C).

The second program (Model 2) makes use of a more sophisticated theory developed by Jones and Bhadeshia[32] in the context of wrought steels. The program involves a better treatment of the nucleation of the variety of phases, and rigorously allows for impingement between different phases. The model is incomplete in that it includes only allotriomorphic ferrite, idiomorphic ferrite, Widmanstätten ferrite and pearlite. It has not been previously applied to welds, but it should in principle give a better calculation of the microstructure. For example, Model 1 does not explicitly include the nucleation of allotriomorphic ferrite (and hence assumes complete coverage of the austenite grain surfaces), whereas Jones and Bhadeshia's model can determine the allotriomorphic ferrite content even when the nucleation rate is very small. Subroutines from the original program,[43] dealing with the nucleation and growth of allotriomorphic ferrite and Widmanstätten ferrite, were therefore incorporated into the first model. It was found in the present work that, because of the extremely low carbon content of the steels used, allotriomorphic and Widmanstätten ferrite were able to continue growing during the cooling cycle even after the onset temperature for bainite formation had been reached. The evolution of bainite was modelled in a similar way to that in Model 1, based on the carbon content of the residual austenite at the bainite start temperature. Transformation of all ferritic and bainitic phases were considered to cease when the composition of the residual austenite reached its martensite start temperature. The fractions of martensite and retained austenite were also evaluated as in Model 1, thus determining the final microstructure including the amount of retained austenite.

The austenite grain size, in a direction normal to that of columnar growth, was measured from optical micrographs of a transverse section. The cooling rate calculations were input into the program in the form given by equation (13). Table 3 gives the welding parameters, the measured grain sizes used to carry out the microstructural calculations and the predicted microstructure for each model in terms of the volume fractions of allotriomorphic ferrite α_f, Widmanstätten ferrite α_w and marteniste. In all cases the volume fraction of bainite and acicular ferrite was predicted to be zero and the amount of retained austenite was less than 0·01. Also given in Table 3 are the cooling times, $t_{8/5}$, the time taken for the weld pool to cool from 800 to 500°C, which indicate the time available for growth of the ferrite phases.

Figure 10 compares the measured hardness value of each spot weld with that calculated using the two models. The experimental hardness values are observed to decrease steadily with increasing laser on time, and consequently, cooling time. Model 1, however, fails to predict any allotriomorphic or Widmanstätten ferrite at all for low laser on times, and then jumps to predicting high volume fractions for both types of ferrite at higher laser on times. The predicted hardness is too high at low on times and too low at high on times. The reason for the jump is the failure of the model to consider the possibility of incomplete

Table 3 Predicted volume fractions of austenite decomposition products in fusion zone of spot welds: prior austenite grain size and cooling time $t_{8/5}$ used in calculations are also given

				Model 1			Model 2		
Power, kW	On time, s	$t_{8/5}$, s	Grain size, μm	α_f,%	α_w,%	Martensite, %	α_f,%	α_w,%	Martensite, %
1·0	0·15	0·07	22	0	0	99	0	0	100
1·0	0·65	0·30	37	0	0	99	1	0	99
1·0	1·15	0·83	41	0	0	99	22	1	77
1·0	1·65	1·21	46	20	61	19	24	4	72
1·0	2·15	1·44	47	31	55	14	25	6	68
1·0	2·65	1·55	62	27	43	30	21	7	72
1·4	0·15	0·08	20	0	0	99	0	0	100
1·4	0·65	0·49	31	0	0	99	15	0	85
1·4	1·15	1·09	37	0	0	99	27	3	70
1·4	1·65	1·39	44	31	59	9	27	6	67
1·4	2·15	1·54	53	30	49	20	24	8	69
1·4	2·65	1·60	54	31	48	21	23	8	68
2·23	0·15	0·22	22	0	0	99	0	0	99
2·23	0·165	0·25	24	0	0	99	0	0	99
2·23	0·180	0·30	22	0	0	99	1	0	98
2·23	0·195	0·34	24	0	0	99	2	0	97
2·23	0·210	0·42	27	0	0	99	8	0	91
2·23	0·225	0·50	26	0	0	99	16	1	83

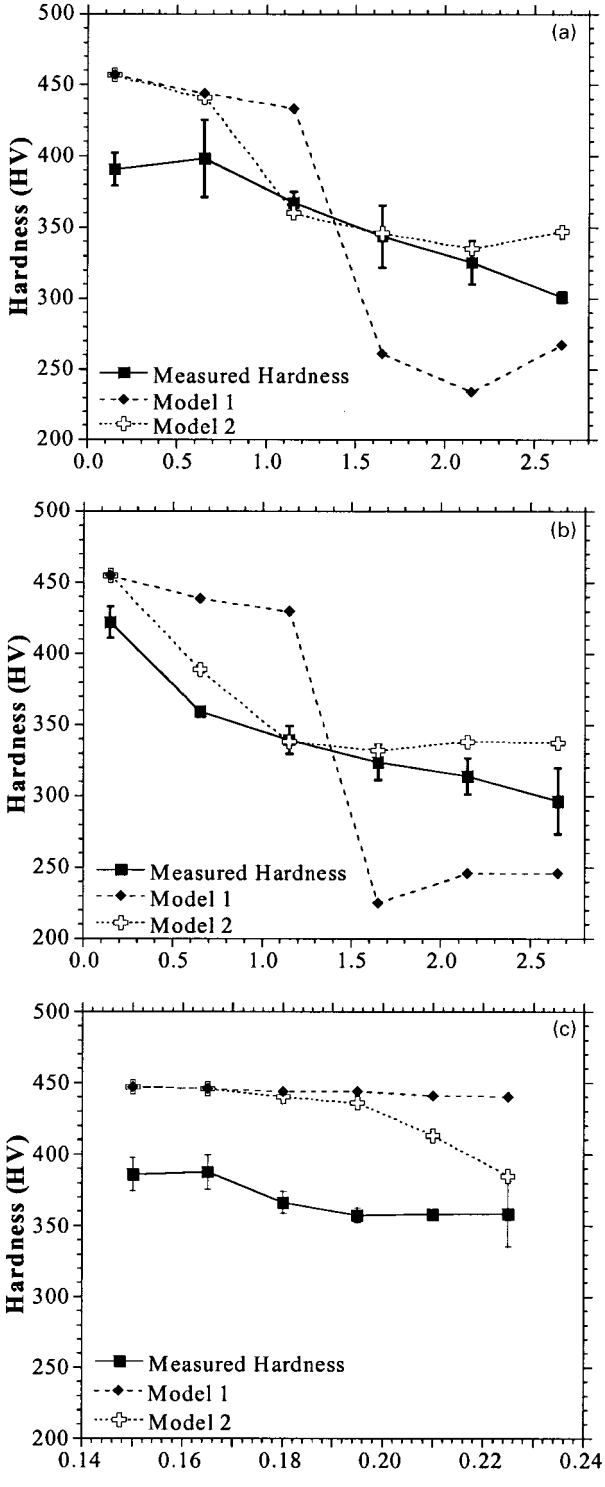

a 1·0 kW; *b* 1·4 kW; *c* 2·23 kW

10 Comparison of predicted and measured weld pool hardness for given laser powers

coverage of the grain boundaries during growth. This is particularly important when the grain size is small, as is the case here, but becomes less of a problem as the grain size increases. The predicted hardness values given by Model 2, however, are a much better indication of the corresponding experimental values, particularly for the 1·0 and 1·4 kW spot welds. The measured hardness values of the spot welds at 2·23 kW are significantly lower than predicted. A comparison of the observed microstructure (Fig. 8*g*–8*i*) with the calculated microstructure in Table 3 shows some discrepancies. Model 1 predicts no ferrite at all. Model 2 predicts no allotriomorphic ferrite at the lowest on time, although a small amount is clearly observed in Fig. 8*g*, and predicts only 1% Widmanstätten ferrite at the highest on time, although significant amounts are present in the microstructure (Fig. 8*i*).

There are several factors that may contribute to the discrepancies between the observed and calculated hardness and microstructure. First, the accuracy of the microstructure model; although Jones and Bhadeshia showed that the model gave reasonable overall results with measured values in wrought steels, the error in the volume fraction of each transformation product could be as much as 0·2.[32] Second, the hardness of martensite is very sensitive to the carbon concentration.[27] Variations in carbon concentration in the metal will affect the hardness of any martensite produced in the microstructure. Third, the accuracy of the predicted cooling rates; it can be seen from Figs. 9 and 10 that the hardness values predicted by Model 2 are in good agreement with the measured values at higher laser on times, while at lower on times the estimated hardness is greater than that observed through experiments. This may indicate the prediction of too high a cooling rate at low on times, as a result of the neglect of convective and radiative heat transfer from the laser beam and the vapour plasma inside the weld pool in the thermal analysis. The presence of vapour plasma, in reality, possibly sets a much higher temperature gradient between the weld pool and the surrounding material. This becomes a major driving force for heat transfer, resulting in the surrounding material attaining a higher temperature compared to that obtained in the present analysis, particularly at lower on times of 0·15 or 0·65 s. However, at higher on times, the weld pool size increases considerably and the surrounding material attains relatively higher temperatures, reducing the temperature gradient between the weld pool and surrounding material and leading to lower cooling rates. It is therefore conceivable that for a more accurate prediction of the weld pool microstructure, a further refinement of the thermal analysis is required which takes into account the presence of the vapour phase inside the weld pool. However, the present authors prefer to treat these as speculations since in the absence of actual cooling data, it is not possible to distinguish between a potential error in the calculated cooling rate and a possible error in the estimation of hardness. On the whole, the agreement between experiment and theory is rather good given the complexity of the analysis.

CONCLUSIONS

Thermal and microstructural analyses have been used in combination to understand the development of laser spot welds in sheet steel. The thermal analysis is based on heat conduction and a representation of the beam as a double-ellipsoidal heat source. The microstructural analysis takes the calculated cooling rate as an input into phase transformation theory to estimate the microstructure and uses microstructure–property relationships to estimate the corresponding weld metal strength and hardness value. The influence of parameters like laser power and on time on the estimation of microstructure and hardness have also been evaluated. A satisfactory agreement between the measured and estimated hardness has been obtained especially for higher laser on times.

ACKNOWLEDGEMENTS

The authors wish to acknowledge the financial support provided by the British Council, UK, and the Department of Science and Technology, India under the scheme UK–India Science and Technology Research Fund (UISTRF). Dr Walsh would like to thank ABB A.G., Germany, for financial support and for the weld samples.

REFERENCES

1. H. B. KIM and C. H. LEE: *Sci. Technol. Weld. Joining*, 1999, **4**, (1), 51–57.
2. W. M. YIP, H. C. MAN and W. H. IP: *Sci. Technol. Weld. Joining*, 1999, **4**, (4), 226–232.
3. T. NARIKIYO, H. MIURA, S. FUJINAGA, H. TAKENAKA, A. OHMORI and K. INOUE: *Sci. Technol. Weld. Joining*, 1999, **4**, (5), 302–307.
4. J. TUSEK and M. SUBAN: *Sci. Technol. Weld. Joining*, 1999, **4**, (5), 308–311.
5. J. DU, J. LONGOBARDI, W. P. LATHAM and A. KAR: *Sci. Technol. Weld. Joining*, 2000, **5**, (5), 304–309.
6. U. TANRIVER, J. LONGOBARDI, W. P. LATHAM and A. KAR: *Sci. Technol. Weld. Joining*, 2000, **5**, (5), 310–316.
7. M. KOÇAK, J. DOS SANTOS and S. RIEKEHR: *Sci. Technol. Weld. Joining*, 2001, **6**, (6), 347–350.
8. C. J. PAGE, T. DEVERMANN, J. BIFFIN and N. BLUNDELL: *Sci. Technol. Weld. Joining*, 2002, **7**, (1), 1–10.
9. D. E. SWIFT-HOOK and A. E. F. GICK: *Weld. J.*, 1973, **52**, (11), 492s–499s.
10. G. J. ANDREWS and D. R. ATTHEY: *J. Appl. Phys. D*, 1976, **9**, 2181–2194.
11. E. A. METZBOWER: *Weld. J.*, 1990, **69**, (7), 272s–278s.
12. A. KAPLAN: *J. Appl. Phys. D*, 1994, **27**, 1805–1814.
13. W. GUO and A. KAR: *Sci. Technol. Weld. Joining*, 2000, **5**, (5), 317–323.
14. J. MAZUMDAR and W. M. STEEN: *J. Appl. Phys. D*, 1980, **5**, (2), 941–947.
15. A. PAUL and T. DEBROY: *Metall. Trans. B*, 1988, **l9**, 851–858.
16. T. ZACHARIA, S. A. DAVID, J. M. VITEK and T. DEBROY: *Metall. Trans. A*, 1989, **20**, 957–967.
17. T. ZACHARIA, S. A. DAVID, J. M. VITEK and T. DEBROY: *Weld. J.*, 1989, **68**, (12), 499s–509s.
18. W. S. CHANG and S. J. NA: *J. Mater. Process. Technol.*, 2002, **120**, 208–214.
19. J. GOLDAK, A. P. CHAKRAVARTI and M. BIBBY: *Metall. Trans. B*, 1984, **l5**, 229–305.
20. J. GOLDAK, M. BIBBY, J. MOORE, R. HOUSE and B. PATIL: *Metall. Trans. B*, 1986, **17**, 587–600.
21. M. R. FREWIN and D. A. SCOTT: *Weld. J.*, 1999, **78**, (1), 15s–22s.
22. H. K. D. H. BHADESHIA and L.-E. SVENSSON: in 'Mathematical modelling of weld phenomena', (ed. K. E. Easterling and H. K. D. H. Bhadeshia), 109–182; 1993, London, Institute of Materials.
23. H. K. D. H. BHADESHIA, L.-E. SVENSSON and B. GRETOFT: *J. Mater. Sci. Lett.*, 1985, **4**, 305–308.
24. H. K. D. H. BHADESHIA, L.-E. SVENSSON and B. GRETOFT: *Acta Metall.*, 1985, **33**, (7), 1271–1283.
25. B. GRETOFT, H. K. D. H. BHADESHIA and L.-E. SVENSSON: *Acta Stereol.*, 1986, **5**, (1), 365–371.
26. L.-E. SVENSSON, B. GRETOFT and H. K. D. H. BHADESHIA: *Scand. J. Metall.*, 1986, **15**, 97–103.
27. J. C. ION, K. E. EASTERLING and M. F. ASHBY: *Acta Metall.*, 1984, **32**, 1949–1962.
28. M. TAKAHASHI and H. K. D. H. BHADESHIA: *Mater. Trans. JIM*, 1991, **32**, 689–696.
29. D. P. KOISTINEN and R. E. MARBURGER: *Acta Metall.*, 1959, **7**, 59–60.
30. A. A. B. SUGDEN and H. K. D. H BHADESHIA: *Metall. Trans. A*, 1988, **19**, 1597–1602.
31. C. H. YOUNG and H. K. D. H. BHADESHIA: *Mater. Sci. Technol.*, 1994, **10**, 209–214.
32. S. J. JONES and H. K. D. H. BHADESHIA: *Acta Metall.*, 1997, **45**, (7), 2911–2920.
33. S. S. BABU, S. A. DAVID, J. M. VITEK, K. MUNDRA and T. DEBROY: *Mater. Sci. Technol.*, 1995, **11**, 186–199.
34. E. A. METZBOWER, H. K. D. H. BHADESHIA and R. H. PHILLIPS: *Mater. Sci. Technol.*, 1994, **10**, 56–59.
35. E. A. METZBOWER, D. W. MOON, P. E. DENNEY and R. H. PHILLIPS: 'Welding metallurgy of structural steels', (ed. J. Y. Koo), 481–497; 1987, Warrendale, PA, TMS-AIME.
36. T. ZACHARIA, J. M. VITEK, J. A. GOLDAK, T. A. DEBROY, M. RAPPAZ and H. K. D. H. BHADESHIA: *Model. Simul. Mater. Sci. Eng.*, 1995, **3**, 265–288.
37. A. DE: *Sci. Technol. Weld. Joining*, 2002, **7**, (2), 119–124.
38. A. DE, S. K. MAITI, C. A. WALSH and H. K. D. H. BHADESHIA: *Sci. Technol. Weld. Joining*, 2002 to be published.
39. C. A. WALSH, H. K. D. H. BHADESHIA, A. LAU, B. MATTHIAS, R. OESTERLEIN and J. DRECHSEL: *J. Laser Appl.*, 2003, **15**, (2), 68–76.
40. A. A. B. SUGDEN and H. K. D. H. BHADESHIA: *Mater. Sci. Technol.*, 1989, **5**, 977–984.
41. H. S. CARSLAW and J. C. JAEGER: 'Conduction of heat in solids', 2nd edn, 258; 1960, Oxford, Clarendon Press.
42. Internet: http://www.msm.cam.ac.uk/map/, Materials Algorithms Project, Cambridge University, Cambridge, UK.
43. Internet: http://www.msm.cam.ac.uk/map/, Program 'MAP_STEEL_STRUCTURE', Cambridge University, Cambridge, UK.